Journal of the European Ceramic Society 41 (2021) 5056–5065

Contents lists available at ScienceDirect

Journal of the European Ceramic Society

journal homepage: www.elsevier.com/locate/jeurceramsoc

Additive manufacturing of silicon carbide by selective laser sintering of PA12 powders and polymer infiltration and pyrolysis

Marco Pelanconi [a,b,*], Paolo Colombo [b,c], Alberto Ortona [a]

[a] University of Applied Sciences (SUPSI-DTI), Mechanical Engineering and Materials Technology Institute (MEMTi), Polo Universitario Lugano, 6962, Lugano, Switzerland
[b] Department of Industrial Engineering, University of Padova, 35131, Padova, Italy
[c] Department of Materials Science and Engineering, The Pennsylvania State University, University Park, PA, 16802, USA

ARTICLE INFO

Keywords:
Additive manufacturing
Silicon carbide
SLS
PIP
Infiltration
Preceramic polymers

ABSTRACT

In this work, we propose a novel hybrid additive manufacturing technique, which combines selective laser sintering (SLS) of polyamide powders and subsequent preceramic polymer infiltration and pyrolysis to manufacture Silicon Carbide components for complex architectures. By controlling the porosity of the sintered polymeric preform we are able to control the shrinkage upon the first infiltration and pyrolysis. This enabled the manufacturing of smaller features than those achievable with other manufacturing techniques. The mechanical strength of the resulting ceramic increased with the number of reinfiltration cycles up to 24 MPa, inversely the residual porosity decreased to 10 vol%. The microstructure showed two distinct phases of SiOC and SiC. The first was attributed to the interaction between the porous polyamide and the ceramic precursor during the first infiltration. SiC derived from the pyrolysis of the preceramic precursor alone.

1. Introduction

Additive manufacturing (AM) of complex ceramic architectures [1–3] has strongly increased in the last years due to the technology advancements both in the equipment and the constituent materials [4–6]. Among the non-direct manufacturing techniques available the best improvements were obtained thanks to new 3D printing equipment appearing on the market. They are able to handle liquid or solid beds in a better way to achieve high parts resolution with unprecedented powder packing. The acceleration in parts production started first with the most common oxide-based ceramics [7]. For those materials several components have been successfully manufactured for biomedical applications (bones, teeth) [8,9], heterogeneous catalysis [10,11], concentrated solar energy [12], water filters [13], heat management [14,15], porous burners [16,17], automotive [18]. These components were produced mainly by stereolithography (SLA) [19–21]. This technique is successful for many oxide powders because of their favourable optical characteristics. Non oxide ceramics are difficult to process in this way because such ceramic powders are in general opaque, absorbing or reflective against UV light, not allowing proper photocuring of the photopolymer. Few examples of non oxide ceramic green forming by stereolithography are present into the literature: some parts were produced in silicon nitride [22]. To the best of the authors' knowledge, only a few examples exist of stereolithography of photocurable slurries in which silicon carbide (SiC) powders were dispersed [23,24]. On the other hand, several works have been carried out on stereolithography 3D printing of silicon carbide parts using preceramic precursor mixed with photocurable polymers [25–28].

Other techniques, hybridizing additive manufacturing for polymers with conventional processing routes for ceramics have been also developed [29–31]. They include: polymer template 3D printing followed by replica [32,33], 3D printing of a polymer template followed by polymer infiltration and pyrolysis (PIP) [34,35], template 3D printing by binder jetting and pyrolysis followed by polymer infiltration and pyrolysis [36–38], chemical vapour deposition/infiltration [39–41] or reactive silicon infiltration [42–44]. There is also an interesting application employing selective laser sintering (SLS) on dry silicon carbide-silicon powders beds. Silicon is used as binding phase for the silicon carbide powders. It is further converted by reaction bonding into silicon carbide by providing extra carbon to the preform [45]. These techniques have all advantages and disadvantages. Among the advantages, some of them are easy to use and already industrialised, such as the replica method [46] and some of them can realize high precision parts. Regarding the disadvantages, in the replica approach it is not

* Corresponding author.
E-mail address: marco.pelanconi@supsi.ch (M. Pelanconi).

https://doi.org/10.1016/j.jeurceramsoc.2021.04.014
Received 5 March 2021; Received in revised form 7 April 2021; Accepted 8 April 2021
Available online 16 April 2021

possible to achieve high resolution in complex ceramic architectures, and parts (e.g. struts of cellular structures) are hollow. For direct stereolithography of photocurable polymers and SiC powders, the main drawback is the opacity of the powders, which does not allow for high powder packing.

We propose in this paper a new hybrid approach that exploits SLS of polymeric powders combined with polymer infiltration and pyrolysis (PIP). The significant advantage of this approach, beside the maturity and cost of SLS with thermoplastic powders, is the possibility to control the microporosity of the plastic preform by adjusting several SLS parameters. By tuning the preform microporosity, we were able to control the amount of preceramic polymer that infiltrates the preform during the first impregnation cycle and thus, due to the different ceramic yield of the thermoplastic polymer and the preceramic polymer, to control the shrinkage of the preform after the first pyrolysis step.

In this work, we concentrated on manufacturing bulk components. We believe that knowing which the constituent material properties are will assist in further designing and manufacturing complex ceramics artefacts to be then convert into silicon carbide through the above-mentioned hybrid approach. This process will allow for the manufacturing of complex SiC periodic architectures with fine resolution and smaller unit cells than those developed to date.

2. Materials and methods

Selective Laser Sintering 3D printing was employed to manufacture a high-porous polymeric preform which underwent some cycles of infiltration with a preceramic polymer and subsequent pyrolysis at 1000 °C in inert atmosphere. Fig. 1 shows a schematic of the process principle. High microporosity of the polymeric preform is essential for a better precursor infiltration and therefore a more effective conversion into SiC after each step.

2.1. Materials

Two materials were employed for the fabrication of the final ceramic part: (i) polyamide (Nylon12) powder (PA12, Sintratec AG, Brugg, Switzerland) and (ii) allylhydridopolycarbosilane (AHPCS) preceramic polymer (StarPCS™ SMP-10, Starfire Systems Inc, Glenville, NY, USA). Black spherical powder (D_{50}: 60 μm) of PA12 was used for the 3D printing of the polymeric preform. PA12 is a thermoplastic and semicrystalline-crystalline material suitable for processing with the SLS technique, with a density of 1.0 g/cm^3. Varying the parameters of the SLS process enables the customization of the microstructure and properties of the finished product. AHPCS liquid precursor to silicon carbide was used for the infiltration of the polymeric preform and to yield the final SiC product after the thermal treatment. The density is 0.998 g/cm^3 and the dynamic viscosity is 40–100 cP s at 25 °C. Amorphous (glassy) SiC forms when pyrolyzing at 850−1200 °C in inert atmosphere, with a 72–78 % of ceramic yield.

2.2. SLS and PIP manufacturing of the materials

2.2.1. 3D printing of the polymeric preform

SLS 3D printing (Sintratec KIT, Sintratec AG, Brugg, Switzerland) was employed for the production of the polymeric preform: by means of a movable laser beam (wavelength: 445 nm; spot size: 250 μm), PA12 powder was selectively sintered locally, layer-by-layer by solidifying a slice of the object. The printing process was performed in air and it involved six phases: (i) the STL model of the part was sliced into two-dimensional cross-sections; (ii) the printing parameters were defined and uploaded in the machine; (iii) the powder bed was heated to reach and maintain a uniform temperature within the PA12 sintering window (Fig. 2A), in order to optimize the energy required by the laser; (iv) the laser started tracing the component section providing thermal energy to locally sinter of the powders; (v) once the slice was scanned, the printing platform was lowered by a pre-set distance and the delivery platform was uplifted; (vi) the recoating blade deposited a new powder layer.

The goal of our work was to select the proper printing parameters, because they affect the sintering rate of the powders and thus the micro porosity of the bulk material. Fully or partially sintering influences the microstructure morphology and therefore the final properties of the component, such as the relative density and mechanical strength. Poor sintering leads to low relative density and vice versa. Table 1 shows the ranges of the “open parameters” of the Sintratec KIT, which can be varied and combined. A screening phase was performed using Design of Experiments (DoE) method (Design-Expert 10.0, Stat-Ease, Minneapolis, MN 55413, USA) in order to reduce the parameters range.

Laser speed (v), layer thickness (z) and powder surface temperature (T_b) were chosen for the optimization DoE analysis (see Figure S1-S2), in order to find the combination that allowed manufacturing low relative density preforms with excellent quality and resolution, easy to clean and to handle. High porosity is essential for a higher infiltration of the preceramic precursor and therefore for obtaining a higher solid content after pyrolysis. Parallelepipeds (8 × 6 ×3 mm^3) were printed and characterized. A total number of 72 print jobs were performed with three replicas for each sample. Finally, the optimal combination of v, z and T_b was used to manufacture cylindrical samples (30 mm diameter, 6 mm thickness). They were then subjected to precursor infiltration and thermal treatment as described in the following paragraphs). Forty samples were printed and densified to understand the material behaviour during the different phases of the process and during the pyrolysis cycles.

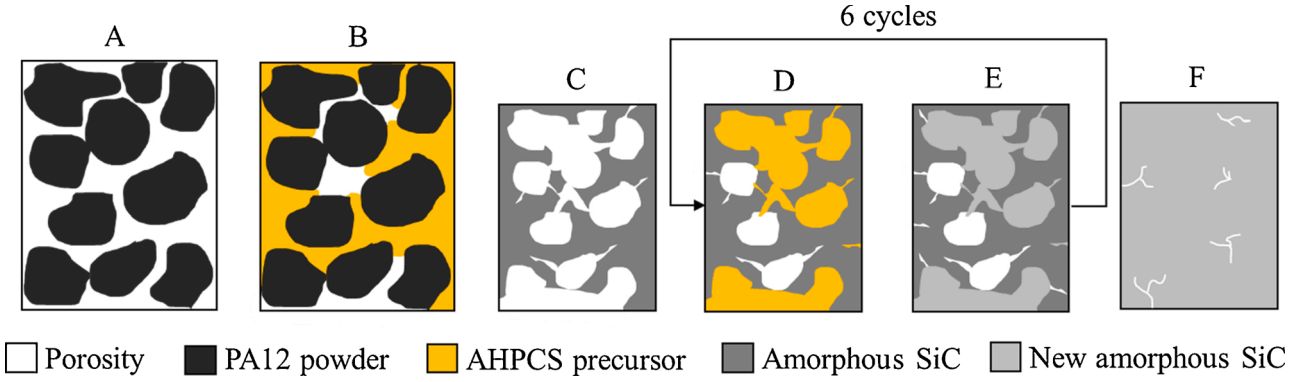

Fig. 1. Schematic of the novel hybrid AM process: (A) 3D printing of the polymeric preform with controlled relative density; (B) preceramic precursor infiltration; (C) pyrolysis; (D) additional infiltration (6 cycles); (E) additional pyrolysis; (F) final ceramic material.

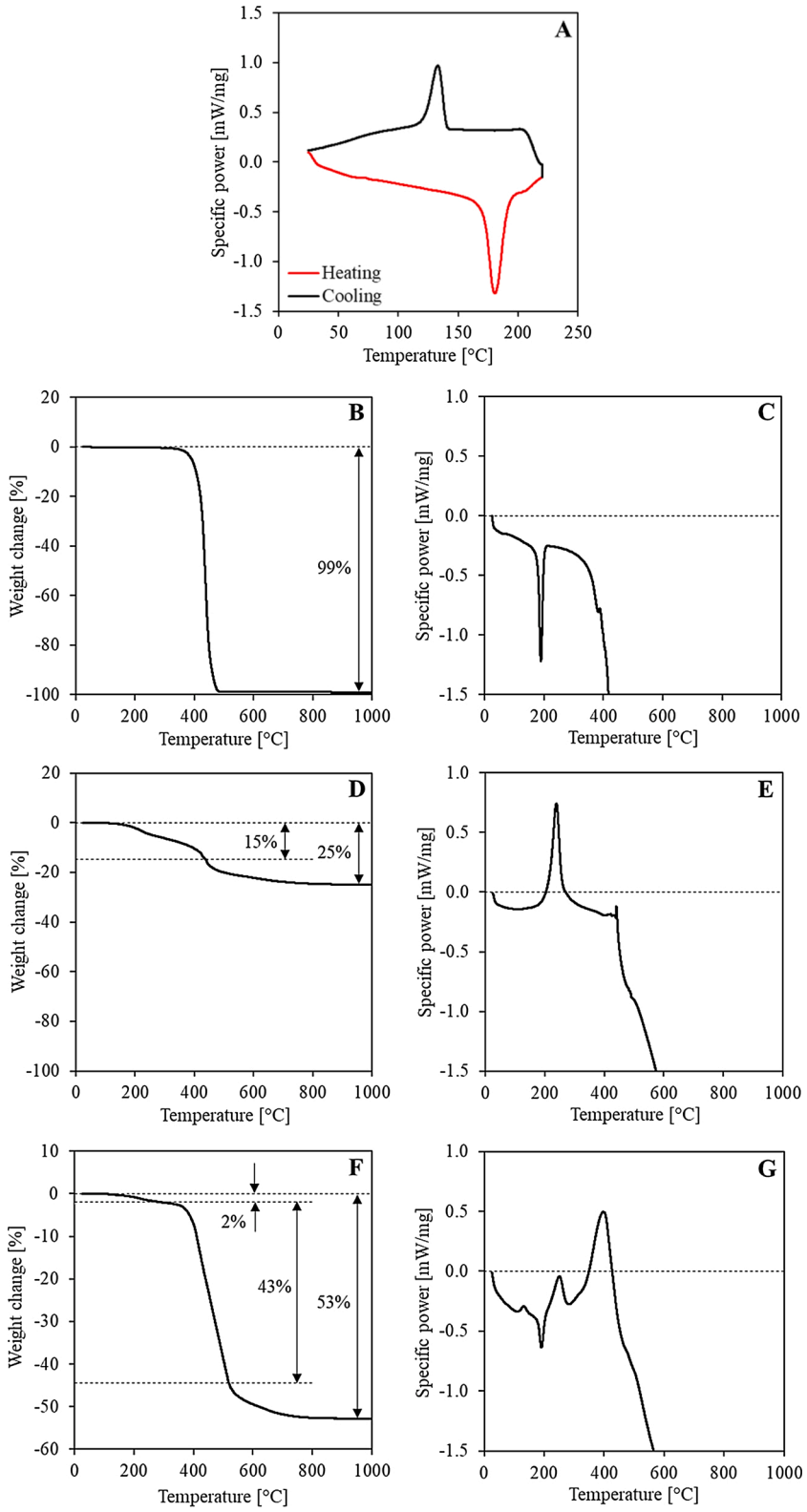

Fig. 2. TGA/DSC analysis: (A) DSC plot for PA12 in Air; (B)-(C) TGA-DSC plot for PA12 in Argon; (D)-(E) TGA-DSC plot for AHPCS in Argon; (F)-(G) TGA-DSC plot for PA12 + AHPCS in Argon (sample infiltrated one time).

Table 1
Ranges of the open parameters of Sintratec KIT, and screening result.

Parameters	Unit	Default range	Screening result
Laser speed (v)	mm/s	1–1000	600–1000
Layer thickness (z)	μm	50–500	100–200
Powder surface temperature (T_b)	°C	20–180	155–170
Chamber temperature	°C	20–150	140
Hatching spacing	μm	1–500	250
Number of perimeters	–	0–3	1
Perimeters offset	μm	1–500	100
Hatching offset	μm	1–500	120

2.2.2. Precursor infiltration and pyrolysis (PIP)

The obtained samples were infiltrated with the AHPCS liquid precursor using an apparatus developed at SUPSI. This apparatus is a sort of a hermetic container at which bottom is poured the polymer, it allows infiltrating samples of various size, by controlling pressure and time. The infiltration process involved four phases: (i) the specimen, hanging outside the polymer into the thigh container, was degassed at room temperature (RT) for 60 s; (ii) the sample was then dipped into AHPCS and held for 60 s; (iii) atmospheric pressure was restored and the sample kept into the polymer for further 60 s; (iv) the sample was re-emerged and excess polymer drained.

After infiltration, samples underwent heat treatment in high-purity flowing Argon (30 L/h). The thermal cycle included three ramps: (i) RT- 500 °C, with a heating rate of 80 °C h^{-1}; (ii) 500–960 °C with a heating rate of 51 °C h^{-1}; (iii) a dwell of 1 h at 960 °C; (iv) natural cooling to RT. PIP were repeated seven times to obtain the maximum densification of the ceramic cylinders.

2.3. Characterization

After SLS, the polymeric preforms were weighted and measured using a digital caliper in order to calculate their relative density. This operation was performed after each PIP in order to investigate the weight change and the shrinkage of the parts (after the first PIP cycle).

The behaviour of PA12 and AHPCS as a function of temperature was evaluated by Thermogravimetry (TGA) and Differential Scanning Calorimetry (DSC) using a thermal analysis system (TGA/DSC 3+, Mettler-Toledo GmbH, Greifensee, Switzerland), in order to understand the effect of the SLS and pyrolysis processes. The data were recorded with the STARe software package (Thermal Analysis Software, Mettler-Toledo GmbH, Greifensee, Switzerland). Analysis in two different conditions was performed. PA12 was heated and cooled in air (flow rate: 50 mL/min; heating/cooling rate: 10 °C/min) up to 220 °C to determine its sintering window. PA12, AHPCS and PA12 infiltrated with AHPCS (PA12 + AHPCS) were analyzed in inert atmosphere using Argon (flow rate: 50 mL/min; heating rate: 10 °C/min) up to 1000 °C to investigate their behaviour during pyrolysis. The combination of the two materials, PA12 + AHPCS, was obtained by infiltrating a PA12 sample with relative density of 52 % with AHPCS (one infiltration cycle). Three analysis were conducted for each material.

The mechanical strength of the ceramic samples was evaluated through biaxial flexural tests (Zwick Z050, Zwick GmbH & Co.KG, Ulm, Germany) employing the ball-on-three-balls (B3B) setup with stainless steels balls of 13 mm diameter [47–49]. Tests were performed at strain rate of 10^{-3} s^{-1} and a cell load of 5 kN (KAP-S, AST, Dresden, Germany) was used to record the reaction force. The cylinder was placed at the center of the three balls and pre-loaded with a force of 2.5 N. A Poisson's ratio of 0.2 was assumed. Five samples were tested for each PIP cycle.

Scanning electron microscopy (SEM) analyses (JSM-6010PLUS/LA, Jeol Ltd., Japan) were conducted to investigate the microstructure of two sets of samples: (i) four PA12 samples with different relative density and (ii) the samples obtained from the fractured ceramic discs after B3B tests. Surface compositional analysis on selected samples was carried out using the Energy Dispersive X-ray Analysis (EDX) probe attached to the SEM.

Mercury intrusion porosimetry (MIP) tests (PoreMaster 60, Anton Paar Switzerland AG, Buchs, Switzerland) were performed in order to evaluate the bulk porosity, the open pore size distribution and the pore volume. Analyses were performed by using a pressure range from 0.0014 MPa to 414 MPa. The geometric surface of the samples as a function of the number of infiltrations was quantified by MIP.

TGA analyses (TGA/DSC 3+, Mettler-Toledo GmbH, Greifensee, Switzerland) were carried out in Air at atmospheric pressure to determine the oxidation behaviour of the produced ceramic materials. Samples taken from the fractured discs after each PIP cycle were tested with a heating rate of 10 °C min^{-1} up to 1200 °C.

3. Results and discussion

3.1. Thermal behaviour of the starting materials

Fig. 2A shows the DSC data recorded for sample PA12 in Air. The material exhibited a sintering window between the onset of crystallization at 140 °C and the onset of melting at 171 °C. Melting occurs during heating while crystallization occurs during cooling. This range defines the temperatures at which the SLS printer must operate. Furthermore, the thermal analysis system provided three useful parameters related to the material: the melting temperature peak at 181 °C, the melt enthalpy of 87 Jg^{-1} and the specific heat capacity of 1.65 Jg^{-1} $°C^{-1}$.

Fig. 2B-G shows the TGA/DSC plots recorded for samples PA12, AHPCS and PA12 + HPCS in Argon. PA12 behaviour (Fig. 2B-C) undergoes the melting between 175 and 220 °C without weight change, and the decomposes between 280 and 500 °C with a 99 % weight loss. At 960 °C the carbon residue was 1% of the initial weight. The melting peak occurred at 190 °C. AHPCS behaviour (Fig. 2D-E) cross-linked between 100 and 400 °C with 15 % weight loss due to the loss of oligomers, and the polymer-to-ceramic transformation occurred between 440 and 1000 °C, with an additional 10 % weight loss. At 960 °C, the SiC residue (ceramic yield) was 75 % of the initial weight. A cross-linking peak is visible at 239 °C, while the phase change peak occurs at 441 °C [50–52]. The curve for sample PA12 + AHPCS behaviour (Fig. 2F-G) shows melting of PA12 and cross-linking of AHPCS between 100 and 280 °C, with 2% weight loss due to the release of AHPCS oligomers. PA12 decomposed between 280 and 520 °C, and AHPCS underwent ceramization between 520 and 1000 °C, with an additional 8% weight loss. At 960 °C, the total residue was 47 % of the initial weight. The melting peak for PA12 occurred at 191 °C, the cross-linking peak for AHPCS at 250 °C and the decomposition peak for PA12 at 410 °C.

By analytically summing the two separate contributions according to Eq. 1, the PA12 + AHPCS ceramic yield should be 37 %.

$$y_{PA12+AHPCS} = \frac{Mi_{PA12} \times y_{PA12} + Mi_{AHPCS} \times y_{AHPCS}}{Mi_{PA12} + Mi_{AHPCS}} \quad (1)$$

where $y_{PA12+AHPCS}$ is the yield of PA12 + AHPCS, Mi_{PA12} and Mi_{AHPCS} are the initial weights of PA12 and AHPCS respectively, y_{PA12} and y_{AHPCS} are the individual yields of the two materials (1% and 75 % respectively). However, from the TGA results the yield was 47 %, 10 % higher than calculated. This increase could be attributed to the portion of PA12 in direct contact with AHPCS, according to microstructural investigations by SEM and oxidation tests (see later).

3.2. Preform processing

Fig. 3 shows the relative density of the printed PA12 samples as a function of laser speed at different powder surface temperature and layer thickness values. As expected, the highest relative density of 0.66 was obtained with the lower laser speed of 600 mm/s, the higher temperature of 170 °C and the smaller layer thickness of 100 μm. This

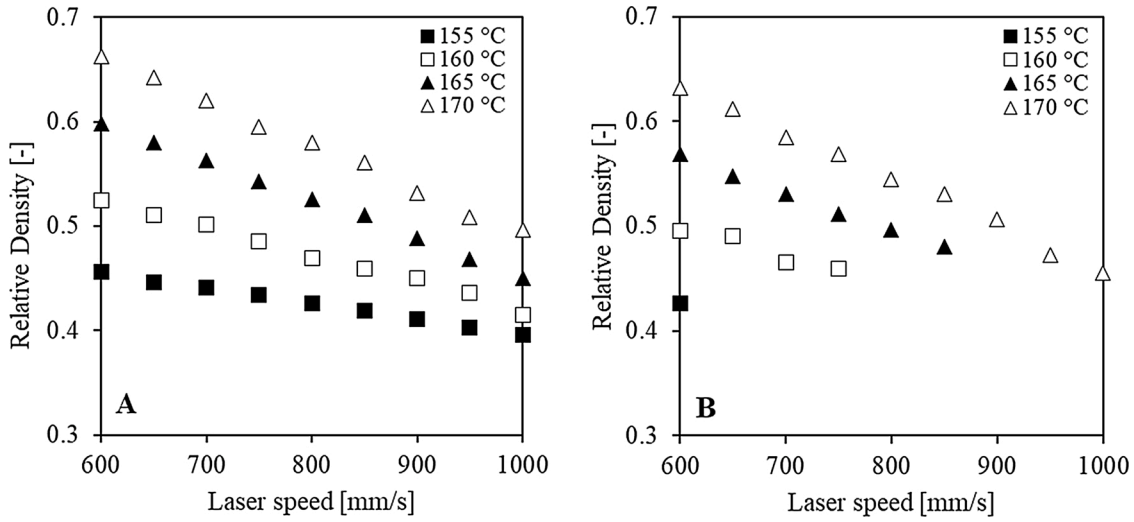

Fig. 3. Relative density of the PA12 printed specimens at different combination of laser speed at different powder surface temperature values and at layer thickness of: (A) 100 μm; (B) 200 μm.

combination of printing parameters allows to provide more thermal energy during printing and consequently to obtain a higher sintering degree of the PA12 particles. Conversely, the relative density decreased with increasing laser speed and decreasing temperature until reaching the lower value at 0.40 with a 100 μm layer thickness. In general, the relative density decreased a layer thickness of 200 μm, but this led to a significant decrease in the mechanical strength and handleability of the parts. Indeed, with the lowest temperature and highest laser speed, the prints failed due to providing insufficient energy for sintering (see Figure S3). The DoE analysis thus allowed to define the optimal parameters for the 3D printing of the polymer preform which was subsequently infiltrated and converted into a ceramic component. The selected parameters were the following: laser speed of 848 mm/s, layer thickness of 100 μm and powder surface temperature of 166 °C. This combination allowed to 3D print solid discs with diameter of 30 ± 0.40 mm and height of 6 ± 0.10 mm, and a relative density of 0.52 ± 0.02 (Fig. 4A).

Infiltration and subsequent pyrolysis of the PA12 discs resulted in the fabrication of SiC porous ceramic samples without shape distortion and macroscopic cracks. The pyrolyzed ceramic discs had a diameter of 23 ± 0.25 mm and a height of 5 ± 0.10 mm. As shown in Fig. 4B, a linear

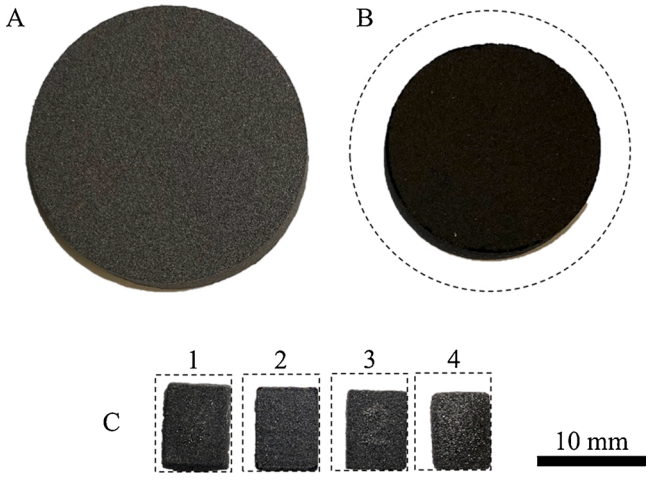

Fig. 4. Optical images of: (A) PA12 sample printed with the selected parameters (relative density of 0.52 before infiltration); (B) part after the first pyrolysis; (C) parts obtained after the first pyrolysis of PA12 samples printed at different relative density values (see Table 2).

Table 2
Relative density (before infiltration) of four PA12 samples produced using different combinations of the printing parameters, and their linear shrinkage after the first pyrolysis.

Sample	v	z	T_b	Rel. Density as printed	Linear shrinkage after pyrolysis
–	mm/s	μm	°C	–	%
1	1000	100	155	0.40	5
2	600	200	155	0.43	15
3	848	100	166	0.52	24
4	600	100	170	0.66	28

shrinkage of 24 % was observed during pyrolysis. This value is correlated to the infiltration rate of the PA12 sample and therefore to its relative density. Four samples with different relative density values were 3D printed in order to investigate their shrinkage. Fig. 4C shows the chosen pyrolyzed samples after the first pyrolysis and Table 2 reports the effect of the printing parameters on the relative density (before infiltration) and the linear shrinkage after the first pyrolysis. Sample 3 is the one manufactured with the optimal parameters previously identified. As result of the pyrolysis, the preform with the lower relative density presented the lower shrinkage. This means that during infiltration, it is possible to fill more volume with the AHPCS and therefore to obtain a higher volumetric fraction of the ceramic phase after pyrolysis. Increasing the relative density of the polymeric preform decreases the infiltrated volume and consequently the shrinkage of the ceramic part increases. By regulating the printing parameters, it is therefore possible to control the size of the ceramic part and this can be very interesting for the production of very small SiC components with high resolution, such as complex cellular architectures.

Table 3
Measured weight and relative density values of the ceramic parts after each PIP cycle.

PIP cycle	Weight	Gain in weight	Rel. Density
–	g	%	–
1	1.65	–	0.30
2	2.30	40	0.59
3	2.72	65	0.80
4	2.99	81	0.79
5	3.18	93	0.82
6	3.32	101	0.85
7	3.42	107	0.90

The pyrolysis of the selected PA12 preform (#3) produced a ceramic part with relative density of 0.30 ± 0.02 after the first pyrolysis. This is due to the PA12 degradation that produced pores inside the part and to the ceramic yield of the AHPCS precursor. In order to increase the relative density, the samples were re-infiltrated six times with liquid AHPCS and then re-pyrolyzed after each infiltration. Table 3 reports the measured weight of the ceramic parts after each PIP cycle and their relative density. During the second cycle, the gain in weight was about 40 % due to the filling of the larger pores and cracks. Increasing the number of cycles, the weight gained increased but at a lower rate. During the last cycle, the gain was much lower than in the other cases and consequently the relative density increases only slightly. This behaviour is due to the strong decrease in the size of the pores and cracks present in the sample, which then becomes very difficult to infiltrate. The final ceramic part, after 7 infiltration and pyrolysis cycles, had a relative density of 0.90 ± 0.01, meaning that the material was not fully dense and therefore micropores and microcracks were still present. By performing seven PIP cycles, the density of the ceramic components doubled.

3.3. Mechanical properties

Stress-strain curves of SiC samples after each PIP cycle are shown in Fig. 5A. In general, the stress increased with increasing strain until the maximum strength was reached, after which the specimens collapsed with brittle fracture. As a result of the fracture, the samples were split into three almost-equal parts. It can be observed that increasing the number of PIP cycles increased the fracture stress and decreases the strain of the samples. Samples pyrolyzed up to three times showed about the half of the maximum stress of the other samples. In Fig. 5B, the strength of the samples as a function of their relative density is shown. The relative density and the average strength increased with increasing the PIP cycles. After the fourth cycle, the increase rate of the relative density was lower meaning that the infiltration was reduced by the drag force of the remaining small pores. Closed pores cannot be filled (see Fig. 6-7PIP). Increasing the infiltration time can definitely increase the infiltration rate of AHPCS, providing a final ceramic part with a higher relative density. After the last cycle, the relative density was still 0.90 showing the limits of PIP processing [50,51,53,54].

3.4. Microstructure

Fig. 6 (1–4) shows the SEM images of the fractured surface of PA12 samples previously presented in Table 2. It is clear that the microstructure of the samples is affected by the sintering rate of the PA12 during SLS. In sample 1, the particles are separated, and few small agglomerates can be observed. The material relative density was 0.40 (before infiltration). In sample 2, more agglomerates of particles can be observed, and the relative density was slightly higher at 0.46. The relative density of sample 3 was about 10 % higher, and a many large agglomerates are visible. Sample 4 shows that the particles are more sintered and large agglomerates are visible all over the cross section. Furthermore, the different fracture behaviour of the four samples can be observed: (i) the fracture of samples 1 and 2 was characterized by the separation of the particles without any breakage of the agglomerates; (ii) the fracture of samples 3 and 4 was characterized by the breakdown of the agglomerates. This is due to the energy that holds the particles together which is related to the energy applied for sintering the powders.

Fig. 6 (1PIP-7PIP) shows the SEM images of the polished fracture surface of the SiC samples after each PIP cycle. By analyzing the composition of the samples, three different phases were found: (i) the black/dark area represents the pores that were in many cases filled with the resin used to incorporate the samples; (ii) the dark grey area is the SiOC produced by the pyrolysis of AHPCS which was directly in contact with the PA12 particles (i.e. the one deriving from the first infiltration); (iii) the light grey area is the SiC produced by the pyrolysis of AHPCS incorporated in subsequent infiltration (cycles 2–7). The polymeric preform was not dried before processing, and therefore we can posit that some adsorbed water was present at their surface during the first infiltration with AHPCS and resulting in the trapping of oxygen molecules [55]. This is confirmed by a 22 % oxygen content in the dark grey phase after EDX analysis, therefore attributable to a SiOC material, while the light grey area had an oxygen content of 9% and thus attributable to a SiC phase (see Table S1). An image analysis was performed in order to further distinguish and quantify the three phases in the SEM images (see Figure S4). Samples 1PIP, 2PIP, 3PIP and 4PIP possessed the three phases in different volumetric fractions: the SiOC phase has a volume fraction of about 15 % in all cases, while the SiC phase increased from 21 % to 55 % and the porosity decreased from 65 % to 29 %. Samples 5PIP, 6PIP and 7PIP showed a different composition due to the large prevalence of SiC in spite of the presence of SiOC: SiC increased from 75 % to 80 %, the porosity decreased from 24 % to 18 % and SiOC occupied only

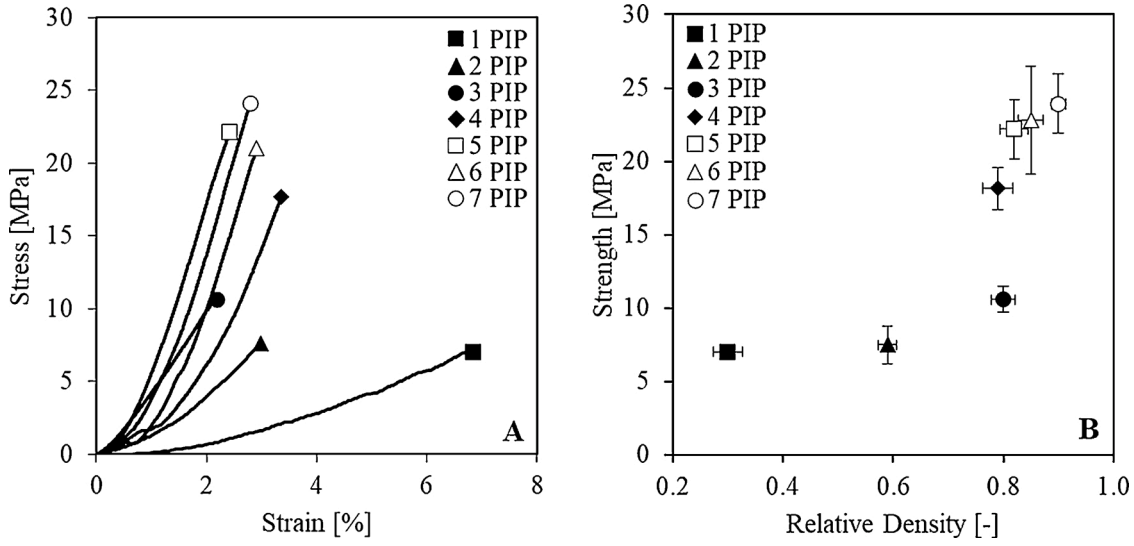

Fig. 5. Mechanical test results for the SiC samples after each PIP cycle: (A) flexural stress-strain curves; (B) average strength as a function of the relative density.

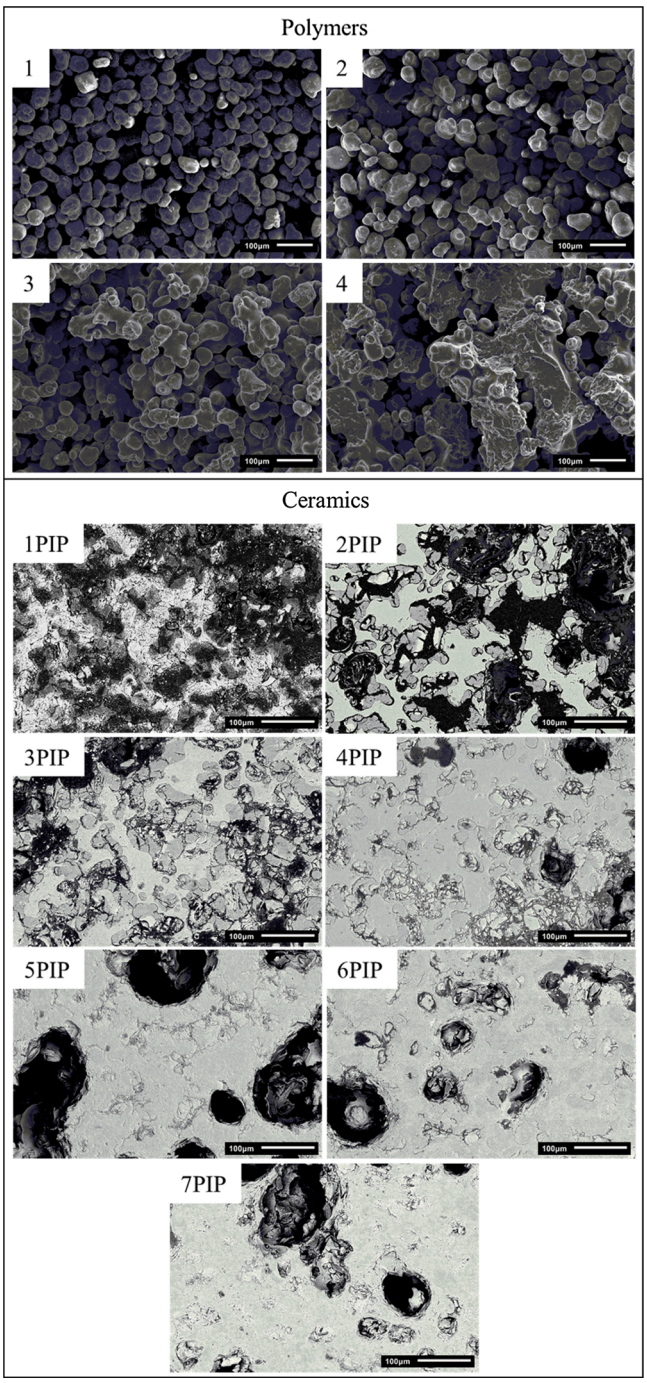

Fig. 6. SEM micrographs: (1-4) Fracture surface of PA12 samples with different relative density; (1PIP-7PIP) Fracture surface of SiC samples after each PIP cycle.

2% of the total volume. However, it is clear that by increasing the number of PIP cycles the volume fraction of pores decreased and the SiC phase greatly increased, as expected, and no additional oxygen contamination appears to have been introduced after the first infiltration cycle, indicating that processing of the AHPCS preceramic polymer in air is possible. Performing more cycles enabled filling the smaller pores (< 50 μm), but not all the large ones. As observed in samples 5PIP, 6PIP and 7PIP, the microstructure is characterized by several pores in the 50−100 μm size range. This is probably due to the effect of capillarity and surface tension, or by the physical impossibility of the polymer to reach those pores. Fig. 6-1PIP shows that after the first pyrolysis cycle, the channels and holes left by the PA12 particles shrunk and their dimensions was smaller than the original particle size. After 3PIP, the material densified until reaching the maximum solid volumetric fraction of 0.90 with the last cycle. Fig. 6-7PIP shows that the microcracks were filled and converted into new SiC, but inside the solid phase there was still residual porosity.

Fig. 7A-C shows the porosimetry results of the PA12 samples previously presented in Table 2. The pore size distribution is plotted against the cumulative pore volume (Fig. 7A) comparing the four specimens. Two common behaviour patterns can be observed: the first pore size range (10−45 μm) is attributed to the inter-agglomerate porosity present between the PA12 sintered regions generated by SLS; the second pore size range (0.004−0.5 μm) comprises the intra-agglomerate porosity present within the individual sintered regions. The results show that the microstructure of the samples is characterized by similar pore size distributions, but different amounts of pores. This means that the sintering rate of the PA12 particles influences the number of pores and not their size [56]. It is clear from Fig. 7B that the inter-agglomerate porosity of the PA12 samples before PIP was controlled by the SLS conditions, while the intra-agglomerate porosity was negligible. Fig. 7C shows the comparison between the relative density obtained from the porosimetry analyses and the one calculated according to equation 2 [57]:

$$\widetilde{\rho} = \frac{\rho}{\rho_{bulk}} \tag{2}$$

Where $\widetilde{\rho}$ is the relative density, ρ_{bulk} is the density of the PA12 powder and ρ is the density calculated by the ratio between the weight and the measured volume of the sample.

Fig. 7D-F reports the porosimetry results of the SiC samples after each PIP cycle taken from the fractured ceramic discs. The pore size distribution is plotted against the cumulative pore volume (Fig. 7D) for seven specimens. The final cumulative volume decreased with increasing of the PIP cycles and accordingly the relative density increased, but the behaviour of the samples is clearly different. The microporosity of sample 1PIP is bimodal: larger pores from 0.1 to 40 μm exist together with smaller pores from 0.004 to 0.05 μm. The two distributions are also distinguishable by observing the changes in the curve slope. Sample 1PIP is the only one that has small pores in large quantity, while the other samples contain only larger pores (Fig. 7E). This means that the second PIP cycle enabled filling the smaller pores and reducing the amount of the larger ones. Fig. 7F shows the comparison between the relative density obtained from the porosimetry analyses against the one calculated using Eq. 2. According to literature [52,58,59]and to helium pycnometer analysis, the value of ρ_{bulk} was set to 2.1 g/cm^3. The difference could be attributed to the excess material attached to the external surface after the pyrolysis, which cannot be removed in order to avoid altering subsequent infiltrations.

3.5. Oxidation tests

Fig. 8 shows the oxidation behaviour of the ceramic specimens tested up to 1200 °C in static air at atmospheric pressure. Two trends were observed: active oxidation of carbon and passive oxidation of silicon carbide. The conditions adopted in this work should cause oxidation according to the reactions [60–64]:

$$C(s) + O_2(g) \rightarrow CO_2(g) \tag{3}$$

$$2SiC(s) + 3O_2(g) \rightarrow 2SiO_2(s) + 2CO(g) \tag{4}$$

Oxidation first occurs on the material's surface exposed to air. Therefore, C oxidations is higher in sample 1PIP and 2PIP, which has free carbon at the surface. This is confirmed by their mass loss. From 3PIP the loss of carbon by active oxidation is hindered by SiC active oxidation. Oxygen progresses much slowly by diffusion into the formed SiO_2 and in the SiC denser core. Another factor is the relationship

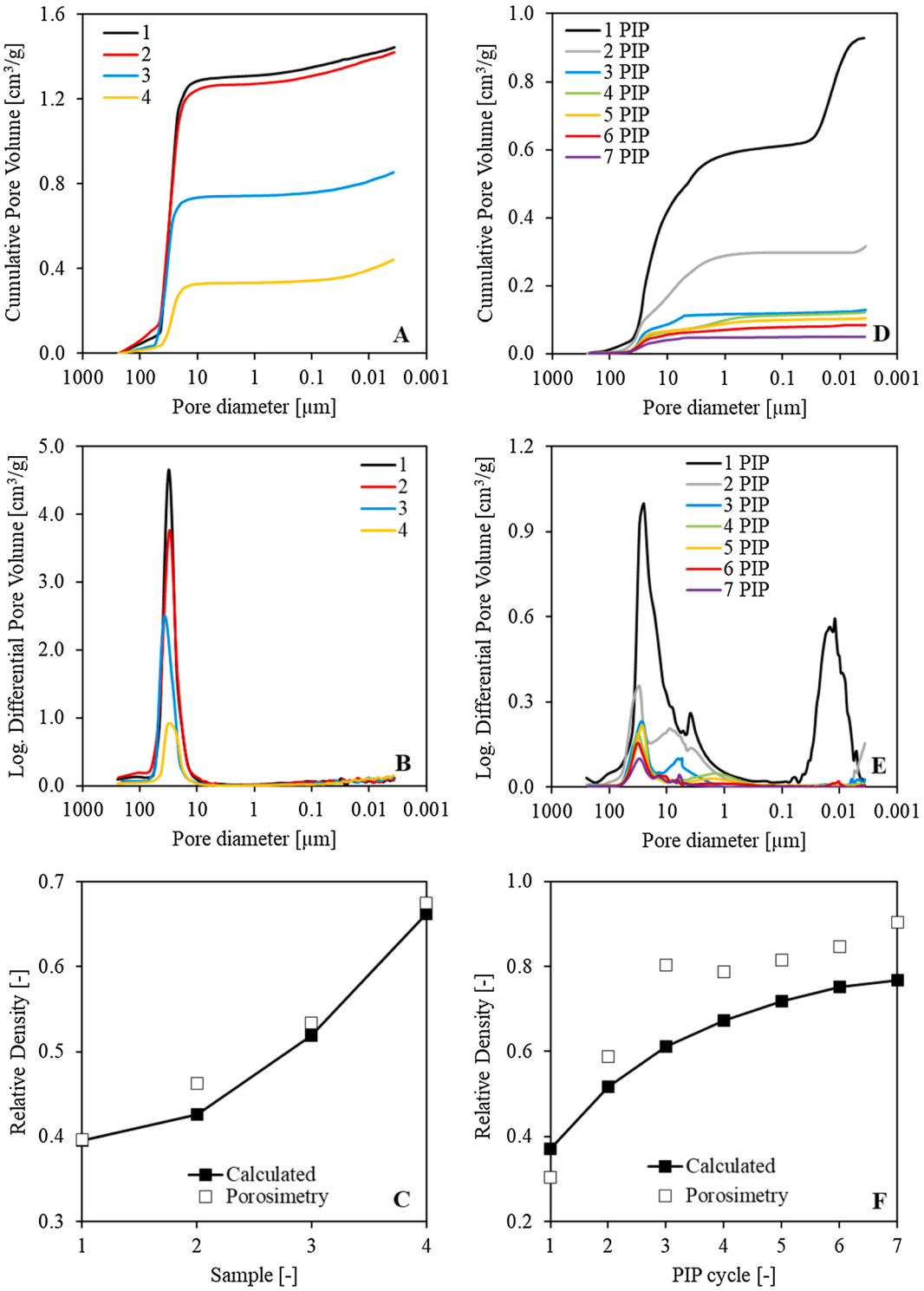

Fig. 7. Porosimetry of PA12 samples (see Table 2): (A) cumulative pore volume and (B) log. Differential pore volume as a function of the pore diameter; (C) relative density for the different specimens. Porosimetry of SiC samples: (D) cumulative pore volume and (E) log. Differential pore volume as a function of the pore diameter; (F) relative density as a function of the PIP cycle.

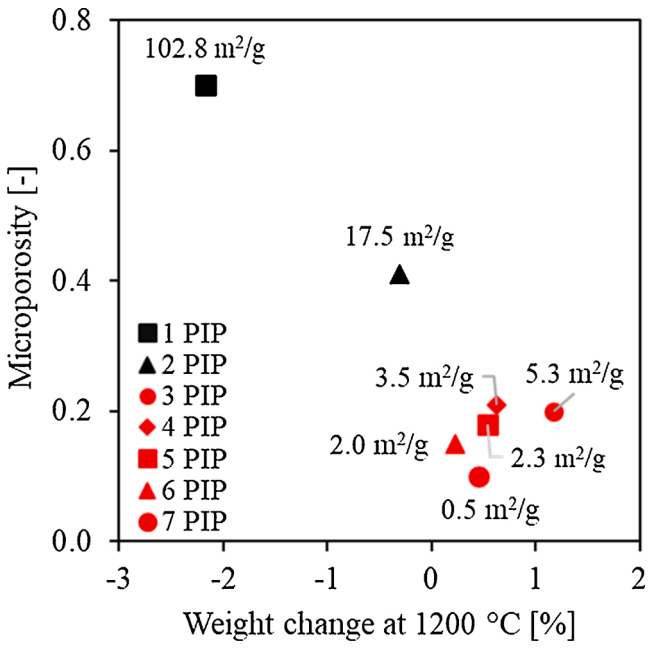

Fig. 8. Oxidation tests of SiC samples performed after each PIP cycle: microporosity as a function of weight change at 1200 °C. Near each point, the amount of geometric surface area of the sample is indicated. Black dots show the prevalence of carbon oxidation and red dots show the prevalence of passive oxidation of SiC.

between the relative density and the geometric surface area of the interconnected pores (open porosity). After the first pyrolysis, the material is highly porous (63 %) and by carrying out several PIP cycles, the porosity decreases due to the filling of the open pores, and moreover some interconnections among pores is eliminated. Consequently, the geometric surface area is reduced allowing less material to be exposed to the oxidation. The weight loss of sample 1PIP corresponds to the amount of the carbon that is oxidized. As the relative density of the material increases, the amount of exposed surface area decreases and the carbon remains trapped inside a SiC matric, while the SiC oxidizes and adds mass to the material due to its passive oxidation. This can be observed also in the SEM results (Fig. 6): by increasing the number of PIP cycles, the products of the first pyrolysis were totally covered by the new SiC phase, resulting in the trapping of carbon inside the matrix. Therefore, the carbon that is first on the surface is oxidized and this prevails over the oxidation of SiC (black data points in Fig. 8), while after carbon is embedded by the new SiC phase with increasing number of infiltrations and is no longer at the surface, the passive oxidation of SiC prevails (red data points in Fig. 8).

4. Conclusions

This study demonstrated that it is possible to obtain SiC components using an indirect Additive Manufacturing approach that employed SLS for the consolidation of a polymeric (polyamide) powder into a part possessing the desired shape and residual porosity. This was then infiltrated a few times (up to 7) using a preceramic polymer precursor (AHPCS), leading to the fabrication of SiC parts.

Key for the success of the AM and PIP processes was the optimization of the printing parameters (in particular, laser speed, layer thickness, powder surface temperature, printing chamber temperature and hatching spacing), which enabled the production of a polymeric preform possessing a suitable degree of interconnected residual porosity (48 vol %), leading to the fabrication of SiC parts with a residual porosity of only ~10 vol% after reinfiltration and pyrolysis.

The strength of the components increased with the number of reinfiltration cycles and the decrease in residual porosity, as expected, and we showed that handling the preceramic precursor in air during infiltration led to only a limited oxygen contamination deriving from environmental humidity.

This optimized manufacturing approach can now be extended to the fabrication of components possessing more complex (e.g. cellular) architectures, leading to parts with much smaller features (e.g. pores) than those achievable using binder jetting or thicker and denser struts than those obtainable through the replica method [32,33] of structures manufactured by Digital Light Processing [65,66].

Declaration of Competing Interest

The authors declare no conflict of interest.

Appendix A. Supplementary data

Supplementary material related to this article can be found, in the online version, at doi:https://doi.org/10.1016/j.jeurceramsoc.2021.04.014.

References

[1] M. Pelanconi, E. Rezaei, A. Ortona, Cellular ceramic architectures produced by hybrid additive manufacturing: a review on the evolution of their design, J. Ceram. Soc. Jpn. 128 (9) (2020) 595–604.
[2] M. Pelanconi, A. Ortona, Review on the design approaches of cellular architectures produced by additive manufacturing, in: M. Meboldt, C. Klahn (Eds.), Industrializing Additive Manufacturing. AMPA 2020, Springer, Cham, 2021, https://doi.org/10.1007/978-3-030-54334-1_5.
[3] G. Bianchi, S. Gianella, A. Ortona, Design and additive manufacturing of periodic ceramic architectures, J. Ceram. Sci. Technol 8 (1) (2017) 59–66.
[4] T. Moritz, S. Maleksaeedi, Additive manufacturing of ceramic components. Additive Manufacturing, Butterworth-Heinemann, 2018, pp. 105–161.
[5] N. Travitzky, A. Bonet, B. Dermeik, T. Fey, I. Filbert-Demut, L. Schlier, et al., Additive manufacturing of ceramic-based materials, Adv. Eng. Mater. 16 (6) (2014) 729–754.
[6] T. Chartier, C. Dupas, M. Lasgorceix, J. Brie, N. Delhote, C. Chaput, Additive manufacturing to produce complex 3D ceramic parts, J. Ceram. Sci. Technol. 6 (2) (2014) 95–104.
[7] O. Santoliquido, P. Colombo, A. Ortona, Additive Manufacturing of ceramic components by Digital Light Processing: A comparison between the "bottom-up" and the "top-down" approaches, J. Eur. Ceram. Soc. 39 (6) (2019) 2140–2148.
[8] R. Galante, C.G. Figueiredo-Pina, A.P. Serro, Additive manufacturing of ceramics for dental applications: a review, Dent. Mater. 35 (6) (2019) 825–846.
[9] A. Bhargav, V. Sanjairaj, V. Rosa, L.W. Feng, Y.H.J. Fuh, Applications of additive manufacturing in dentistry: a review, J. Biomed. Mater. Res. Part B Appl. Biomater. 106 (5) (2018) 2058–2064.
[10] O. Al-Ketan, M. Pelanconi, A. Ortona, R.K. Abu Al-Rub, Additive manufacturing of architected catalytic ceramic substrates based on triply periodic minimal surfaces, J. Am. Ceram. Soc. 102 (10) (2019) 6176–6193.
[11] O. Santoliquido, G. Bianchi, P. Dimopoulos Eggenschwiler, A. Ortona, Additive manufacturing of periodic ceramic substrates for automotive catalyst supports, Int. J. Appl. Ceram. Technol. 14 (6) (2017) 1164–1173.
[12] Q.L. Meng, C.I. Lee, T. Ishihara, H. Kaneko, Y. Tamaura, Reactivity of CeO2-based ceramics for solar hydrogen production via a two-step water-splitting cycle with concentrated solar energy, Int. J. Hydrogen Energy 36 (21) (2011).
[13] R. König, M. Spaggiari, O. Santoliquido, P. Principi, G. Bianchi, A. Ortona, Micropollutant adsorption from water with engineered porous ceramic architectures produced by additive manufacturing and coated with natural zeolite, Journal of Cl. (2020).
[14] M. Pelanconi, M. Barbato, S. Zavattoni, G.L. Vignoles, A. Ortona, Thermal design, optimization and additive manufacturing of ceramic regular structures to maximize the radiative heat transfer, Mater. Des. 163 (2019), 107539.
[15] U. Scheithauer, E. Schwarzer, T. Moritz, A. Michaelis, Additive manufacturing of ceramic heat exchanger: opportunities and limits of the lithography-based ceramic manufacturing (LCM), J. Mater. Eng. Perform. 27 (1) (2018) 1.
[16] A. Ortona, S. Pusterla, P. Fino, F.R.A. Mach, A. Delgado, S. Biamino, Aging of reticulated Si-SiC foams in porous burners, Adv. Appl. Ceram. 109 (4) (2010) 246–251.
[17] S. Gianella, D. Gaia, A. Ortona, High Temperature Applications of Si–SiC Cellular Ceramics, Adv. Eng. Mater. 14 (12) (2012) 1074–1081.
[18] V. Papetti, P.D. Eggenschwiler, A. Della Torre, F. Lucci, A. Ortona, G. Montenegro, Additive manufactured open cell polyhedral structures as substrates for automotive catalysts, Int. J. Heat Mass Transf. 126 (2018) 1035–1036.
[19] R. Felzmann, S. Gruber, G. Mitteramskogler, P. Tesavibul, A.R. Boccaccini, R. Liska, J. Stampfl, Lithography-based additive manufacturing of cellular ceramic structures, Adv. Eng. Mater. 14 (12) (2012) 1052–1058.

[20] J.W. Halloran, Ceramic stereolithography: additive manufacturing for ceramics by photopolymerization, Annu. Rev. Mater. Res. 46 (2016) 19–40.
[21] E. Zanchetta, M. Cattaldo, G. Franchin, M. Schwentenwein, J. Homa, G. Brusatin, P. Colombo, Stereolithography of SiOC ceramic microcomponents, Adv. Mater. 28 (2) (2016) 370–376.
[22] A.A. Altun, T. Prochaska, T. Konegger, M. Schwentenwein, Dense, strong, and precise silicon nitride-based ceramic parts by lithography-based ceramic manufacturing, Appl. Sci. 10 (3) (2020) 996.
[23] G. Ding, R. He, K. Zhang, N. Zhou, H. Xu, Stereolithography 3D printing of SiC ceramic with potential for lightweight optical mirror, Ceram. Int. (2020).
[24] R. He, G. Ding, K. Zhang, Y. Li, D. Fang, Fabrication of SiC ceramic architectures using stereolithography combined with precursor infiltration and pyrolysis, Ceram. Int. 45 (11) (2019) 14006–14014.
[25] Y. de Hazan, D. Penner, SiC and SiOC ceramic articles produced by stereolithography of acrylate modified polycarbosilane systems, J. Eur. Ceram. Soc. 37 (16) (2017) 5205–5212.
[26] C. Vakifahmetoglu, D. Zeydanli, P. Colombo, Porous polymer derived ceramics, Mater. Sci. Eng. R Rep. 106 (2016) 1–30.
[27] P. Colombo, J. Schmidt, G. Franchin, A. Zocca, J. Günster, Additive manufacturing techniques for fabricating complex ceramic components from preceramic polymers, Am. Ceram. Soc. Bull 96 (3) (2017) 16–23.
[28] X. Wang, F. Schmidt, D. Hanaor, P.H. Kamm, S. Li, A. Gurlo, Additive manufacturing of ceramics from preceramic polymers: a versatile stereolithographic approach assisted by thiol-ene click chemistry, Addit. Manuf. 27 (2019) 80–90.
[29] K. Cai, B. Román-Manso, J.E. Smay, J. Zhou, M.I. Osendi, M. Belmonte, P. Miranzo, Geometrically complex silicon carbide structures fabricated by robocasting, J. Am. Ceram. Soc. 95 (8) (2012) 2660–2666.
[30] A. Gómez-Gómez, J.J. Moyano, B. Román-Manso, M. Belmonte, P. Miranzo, M. I. Osendi, Highly-porous hierarchical SiC structures obtained by filament printing and partial sintering, J. Eur. Ceram. Soc. 39 (4) (2019) 688–695.
[31] M. Pelanconi, A. Ortona, Nature-inspired, ultra-lightweight structures with gyroid cores produced by additive manufacturing and reinforced by unidirectional carbon Fiber ribs, Materials 12 (24) (2019) 4134.
[32] P. Jana, O. Santoliquido, A. Ortona, P. Colombo, G.D. Sorarù, Polymer-derived SiCN cellular structures from replica of 3D printed lattices, J. Am. Ceram. Soc. 101 (7) (2018) 2732–2738.
[33] A. Ortona, T. Fend, H.W. Yu, K. Raju, P. Fitriani, D.H. Yoon, Tubular Si-infiltrated SiCf/SiC composites for solar receiver application—Part 1: Fabrication by replica and electrophoretic deposition, Sol. Energy Mater. Sol. Cells (2015).
[34] H. Xiong, L. Zhao, H. Chen, H. Luo, X. Yuan, K. Zhou, D. Zhang, Building SiC-based composites from polycarbosilane-derived 3D-SiC scaffolds via polymer impregnation and pyrolysis (PIP), J. Eur. Ceram. Soc. (2020).
[35] G. Pierin, C. Grotta, P. Colombo, C. Mattevi, Direct Ink writing of micrometric SiOC ceramic structures using a preceramic polymer, J. Eur. Ceram. Soc. 36 (7) (2016) 1589–1594.
[36] I. Polozov, N. Razumov, D. Masaylo, A. Silin, Y. Lebedeva, A. Popovich, Fabrication of silicon carbide fiber-reinforced silicon carbide matrix composites using binder jetting additive manufacturing from irregularly-shaped and spherical powder, Mater. Basel (Basel) (2020).
[37] A. Zocca, P. Lima, S. Diener, N. Katsikis, J. Günster, Additive manufacturing of SiSiC by layerwise slurry deposition and binder jetting (LSD-print), J. Eur. Ceram. Soc. 39 (13) (2019) 3527–3533.
[38] C.L. Cramer, H. Armstrong, A. Flores-Betancourt, L. Han, A.M. Elliott, E. Lara-Curzio, et al., Processing and properties of SiC composites made via binder jet 3D printing and infiltration and pyrolysis of preceramic polymer, Int. J. Cream. Eng. Sci. (2020).
[39] T. Koyanagi, K. Terrani, S. Harrison, J. Liu, Y. Katoh, Additive manufacturing of silicon carbide for nuclear applications, J. Nucl. Mater. 543 (2020), 152577.
[40] A. Baux, A. Goillot, S. Jacques, C. Heisel, D. Rochais, L. Charpentier, et al., Synthesis and Properties of macroporous SiC Ceramics synthesized by 3D printing and chemical vapor infiltration/deposition, J. European Ceram. Soc. (2020).
[41] K. Terrani, B. Jolly, M. Trammell, 3D printing of high-purity silicon carbide, J. Am. Ceram. Soc. 103 (3) (2020) 1575–1581.
[42] H. Zhang, Y. Yang, H. Kehui, B. Liu, M. Liu, Z. Huang, Stereolithography-based additive manufacturing of lightweight and high-strength Cf/SiC ceramics, Addit. Manuf. (2020), 101199.
[43] H. Zhang, Y. Yang, B. Liu, Z. Huang, The preparation of SiC-based ceramics by one novel strategy combined 3D printing technology and liquid silicon infiltration process, Ceram. Int. 45 (8) (2019) 10800–10804.
[44] A. Fleisher, D. Zolotaryov, A. Kovalevsky, G. Muller-Kamskii, E. Eshed, M. Kazakin, V.V. Popov Jr., Reaction bonding of silicon carbides by Binder Jet 3D-Printing, phenolic resin binder impregnation and capillary liquid silicon infiltration, Ceram. Int. (2019).
[45] S. Meyers, L. De Leersnijder, J. Vleugels, J.P. Kruth, Direct laser sintering of reaction bonded silicon carbide with low residual silicon content, J. Eur. Ceram. Soc. 38 (11) (2018) 3709–3717.
[46] A. Ortona, C. D'Angelo, S. Gianella, D. Gaia, Cellular ceramics produced by rapid prototyping and replication, Mater. Lett. 80 (2012) 95–98.
[47] A. Börger, P. Supancic, R. Danzer, The ball on three balls test for strength testing of brittle discs: stress distribution in the disc, J. Eur. Ceram. Soc. 22 (9–10) (2002) 1425–1436.
[48] A. Börger, P. Supancic, R. Danzer, The ball on three balls test for strength testing of brittle discs: part II: analysis of possible errors in the strength determination, J. Eur. Ceram. Soc. 24 (10–11) (2004) 2917–2928.
[49] R. Danzer, W. Harrer, P. Supancic, T. Lube, Z. Wang, A. Börger, The ball on three balls test—strength and failure analysis of different materials, J. Eur. Ceram. Soc. 27 (2–3) (2007) 1481–1485.
[50] M.C. Bruzzoniti, M. Appendini, B. Onida, M. Castiglioni, M. Del Bubba, L. Vanzetti, et al., Regenerable, innovative porous silicon-based polymer-derived ceramics for removal of methylene blue and rhodamine B from textile and Environmental water, Environ. Sci. Pollut. Res. - Int. (2018).
[51] T. Konegger, R. Patidar, R.K. Bordia, A novel processing approach for free-standing porous non-oxide ceramic supports from polycarbosilane and polysilazane precursors, J. Eur. Ceram. Soc. 35 (9) (2015) 2679–2683.
[52] R. Sreeja, B. Swaminathan, A. Painuly, T.V. Sebastian, S. Packirisamy, Allylhydridopolycarbosilane (AHPCS) as matrix resin for C/SiC ceramic matrix composites, Mater. Sci. Eng. B 168 (1–3) (2010) 204–207.
[53] L. Macdonald, Facile fabrication of SiC matrix composites using novel preceramic polymers, Adv. SiC/SiC Ceram. Compos. Developments Appl. Energy Syst. 144 (2006) 87–95.
[54] T.T. Xu, S. Cheng, L.Z. Jin, K. Zhang, T. Zeng, High-temperature flexural strength of SiC ceramics prepared by additive manufacturing, Int. J. Appl. Ceram. Technol. 17 (2) (2020) 438–448.
[55] D. Kwon, E. Park, S. Ha, N. Kim, Effect of humidity changes on dimensional stability of 3D printed parts by selective laser sintering, Int. J. Precis. Eng. Manuf. 18 (9) (2017) 1275–1280.
[56] G.V. Salmoria, C.H. Ahrens, P. Klauss, R.A. Paggi, R.G. Oliveira, A. Lago, Rapid manufacturing of polyethylene parts with controlled pore size gradients using selective laser sintering, Mater. Res. 10 (2) (2007) 211–214.
[57] M.F. Ashby, D. Cebon, Materials selection in mechanical design, Le Journal de Physique IV 3 (C7) (1993) C7–C11.
[58] L.V. Interrante, C.W. Whitmarsh, W. Sherwood, Fabrication of SiC matrix composites by liquid phase infiltration with a polymeric precursor, MRS Online Proc. Library Arch. (1994) 365.
[59] B. Santhosh, E. Ionescu, F. Andreolli, M. Biesuz, A. Reitz, B. Albert, G.D. Sorarù, Effect of pyrolysis temperature on the microstructure and thermal conductivity of polymer-derived monolithic and porous SiC ceramics, J. Europe. (2020).
[60] G.C. D'Amico, A. Ortona, S. Biamino, P. Fino, C. Badini, C. D'Angelo, Oxidation behavior at 1600° C of Si-SiC-ZrB2 composites produced by Si reactive infiltration, Adv. Eng. Mater. 16 (2) (2014) 176–183.
[61] D.J. Park, Y.I. Jung, H.G. Kim, J.Y. Park, Y.H. Koo, Oxidation behavior of silicon carbide at 1200 C in both air and water–vapor-rich environments, Corros. Sci. 88 (2014) 416–422.
[62] E. Rezaei, S. Haussener, S. Gianella, A. Ortona, Early-stage oxidation behavior at high temperatures of SiSiC cellular architectures in a porous burner, Ceram. Int. 42 (14) (2016) 16255–16261.
[63] J.E. Sheehan, Oxidation protection for carbon fiber composites, Carbon 27 (5) (1989) 709–715.
[64] C. Wagner, Passivity during the oxidation of silicon at elevated temperatures, J. Appl. Phys. 29 (9) (1958) 1295–1297.
[65] A. Zambotti, M. Biesuz, R. Campostrini, S.M. Carturan, G. Speranza, R. Ceccato, et al., Synthesis and thermal evolution of polysilazane-derived SiCN (O) aerogels with variable C content stable at 1600° C, Ceram. Int. (2020).
[66] A. Baux, S. Jacques, A. Allemand, G.L. Vignoles, P. David, T. Piquero, et al., Complex geometry macroporous SiC ceramics obtained by 3D-printing, polymer impregnation and pyrolysis (PIP) and chemical vapor deposition (CVD), J. Eur. Ceram. Soc. (2021).